Electronic Supplementary Material (ESI) for Journal of Materials Chemistry C.

Exploring the Influence of Counterions on a Hysteretic Spin-Transition in Isomorphous Iron(II) Complex Salts

Thomas D. Roberts,[a] Christopher M. Pask,[a] Izar Capel Berdiell,[b] Floriana Tuna[c] and Malcolm A. Halcrow*[,a]

[a]*School of Chemistry, University of Leeds, Woodhouse Lane, Leeds LS2 9JT, United Kingdom.*
E-mail: m.a.halcrow@leeds.ac.uk

[b]*Center for Material Science and Nanomaterials (SMN), University of Oslo, Sem Sælands 26, 0371 Oslo, Norway.*

[c]*School of Chemistry and Photon Science Institute, University of Manchester, Oxford Road, Manchester, UK M13 9PL*

Supporting Information

1a·2H₂O

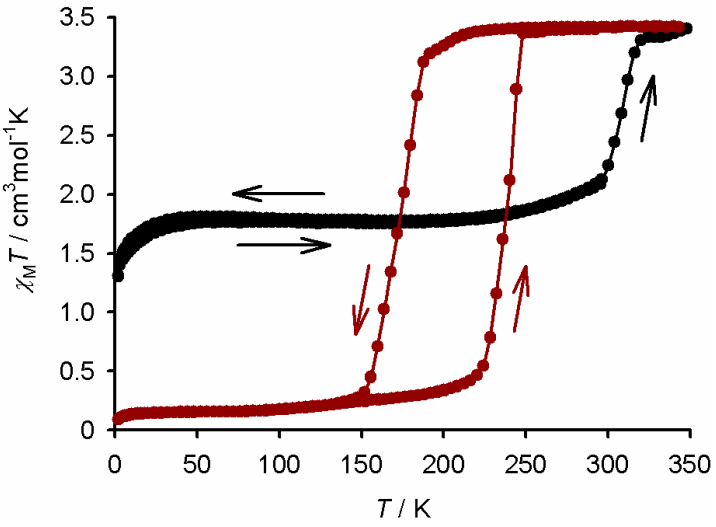

1b·2H₂O

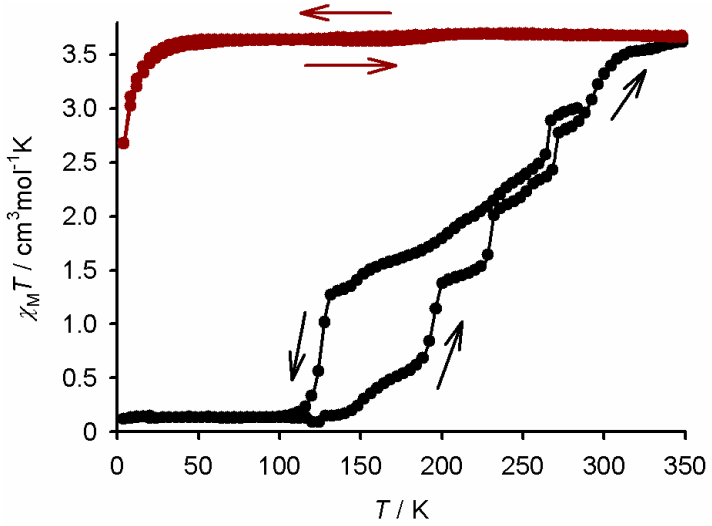

Figure S1 Variable temperature magnetic susceptibility data for **1a**·2H₂O (top) and **1b**·2H₂O (bottom), at a scan rate of 2 K min^{-1}. The data are taken from refs. 1 and 2. An initial 290→5→350 K scan of the as-prepared samples shows their *in situ* dehydration (black), and a 350→5→350 K scan of the dehydrated materials is in red.

Freshly prepared **1a**·2H₂O and **1b**·2H₂O are crystallographically isomorphous at room temperature, while anhydrous **1a** and **1b** are also isomorphous by powder diffraction. However, their spin state properties are very different.

Crystals of **1a**·2H₂O contain a 1:1 high:low-spin population which is retained on cooling, but converts to a fully high-spin state on heating to 350 K following *in situ* loss of lattice water.[1] Dehydrated **1a** (phase B) transforms to a new phase C near 300 K, then exhibits an abrupt spin-transition at $T_{½}$ = 205 K which is associated with another crystallographic phase change.[3] The spin-transition has a 65 K thermal hysteresis loop in the first scan (shown), which narrows to 37 K hysteresis width upon multiple thermal scanning (Figure 4, main article).[1]

In contrast, **1b**·2H₂O exhibits a gradual, highly structured SCO on cooling which involves two crystallographic phase transitions: one just below room temperature, and the other associated with the final hysteretic step near 120 K. The annealed material (phase B) also transforms to phase C around 300 K, but then remains fully high-spin on further cooling.[2]

We unravelled the structural chemistry of **1a** through investigations of its zinc(II) analogue **2a**, whose crystals are more robust during the dehydration process.[3] This study is a continuation of that work, to investigate why **1b** is inactive to SCO despite being isomorphous with **1a**.

Experimental

Synthetic and crystallisation procedures, and analytical characterisation data, for the compounds in this work are presented in the main article.

Single Crystal Structure Analyses

Experimental details of the structure determinations are given in Table S1. All the structures were solved by direct methods *(SHELXS97*[1]), and developed by full least-squares refinement on F^2 (*SHELXL2018*[1]). Crystallographic figures were prepared using *XSEED*.[2] Unless otherwise stated, the following procedures were applied to the refinements. All crystallographically occupied non-H atoms in the following refinements were refined anisotropically, while H atoms were placed in calculated positions and refined using a riding model. Disordered anions were treated with refined Cl–O and O···O distance restraints.

Structure refinements of [Zn*L*$_2$][ClO$_4$]$_2$·2H$_2$O (2b·2H$_2$O) and [Zn*L*$_2$][ClO$_4$]$_2$ (2b). The asymmetric unit of **2b**·2H$_2$O contains one-quarter of a complex dication, with Zn(1) on the $\bar{4}$ site ¾, ¾, ¼ and N(2) and C(5) on the C_2 axis ¾, ¾, *z*. The unique ClO_4^- half-anion is disordered over two sites spanning the C_2 axis ¾, ¼, *z*. These were modelled with occupancies of 0.35 and 0.15. The isotropic displacement ellipsoids of the Cl and O atoms in each partial anion were also constrained to be approximately equal (*SHELXL* SIMU restraint). The unique water half-molecule is crystallographically ordered in this refinement. All non-H atoms except the disordered anion were refined anisotropically, and C- and N-bound H atoms were placed in calculated positions and refined using a riding model. The disordered water H atoms were not located in the Fourier map and are not included in the model, but are accounted for in the molecular weight and density calculations.

Annealing at 350 K for 30 mins on the diffractometer led to dehydration of the crystal. Datasets collected from the **2b** crystal at 350, 300, 250 and 200 K all retained the $P4_2/n$ space group (phase B). The refinement protocol is similar to **2b**·2H$_2$O above, except the unique half-anion was refined over two 0.25-occupied disorder sites. The 200 K structure determination is noisier and less precise than the others, which may reflect its proximity to the phase B→C transition temperature.

At 120 K the crystal has transformed to triclinic phase C. This phase change leads to twinning of the crystals; four twin domains were resolved in the *hkl* file, related by *ca* 90° rotations about the crystallographic *c* axis. Phase C contains just one formula unit of the compound, with all residues on general crystallographic positions. No disorder is present in the phase C refinement.

CCDC-2195223–2195228 contain the supplementary crystallographic data for this paper (Tables S1 and S2). These data can be obtained free of charge from The Cambridge Crystallographic Data Centre via www.ccdc.cam.ac.uk/data_request/cif.

Other measurements

Elemental microanalyses were performed by the microanalytical services at the University of Leeds and London Metropolitan University. ^{1}H NMR spectra employed a Bruker DPX300 spectrometer operating at 300.1 MHz. Magnetic susceptibility measurements were performed on a Quantum Design SQUID or SQUID/VSM magnetometer, with an applied field of 5000 G and a scan rate of 5 Kmin^{-1}. A diamagnetic correction for the sample was estimated from Pascal's constants;[3] a previously measured diamagnetic correction for the sample holder was also applied.

Thermogravimetric analyses (TGAs) were obtained with a TA Instruments TGA Q50 analyser heating at a rate of 10 K min^{-1}under a stream of nitrogen gas, while differential scanning calorimetry (DSC) used a TA Instruments DSC Q20 calorimeter, also with a temperature ramp of 10 Kmin^{-1}. X-ray powder diffraction data were obtained with a Bruker D8 Advance A25 diffractometer using Cu-K_α radiation (λ = 1.5418 Å) .

Table S1 Experimental data for the crystal structure determinations of **2b**·2H$_2$O, before and after *in situ* dehydration.

	2b·2H$_2$O		**2b**, phase B			**2b**, phase C
T / K	120	350	300	250	200	120
molecular formula	$C_{26}H_{30}Cl_2N_{10}O_{10}Zn$	$C_{26}H_{26}Cl_2N_{10}O_8Zn$	$C_{26}H_{26}Cl_2N_{10}O_8Zn$	$C_{26}H_{26}Cl_2N_{10}O_8Zn$	$C_{26}H_{26}Cl_2N_{10}O_8Zn$	$C_{26}H_{26}Cl_2N_{10}O_8Zn$
M_r	778.87	742.84	742.84	742.84	742.84	742.84
crystal class	tetragonal	tetragonal	tetragonal	tetragonal	tetragonal	triclinic
space group	$P4_2/n$	$P4_2/n$	$P4_2/n$	$P4_2/n$	$P4_2/n$	$P\bar{1}$
a / Å	9.6587(2)	9.5847(3)	9.5643(1)	9.5298(3)	9.5249(9)	9.5028(8)
b / Å	–	–	–	–	–	9.5342(9)
c / Å	18.0240(8)	18.4386(11)	18.4259(5)	18.3840(9)	18.346(3)	18.0673(12)
α / °	–	–	–	–	–	80.147(7)
β / °	–	–	–	–	–	84.097(7)
γ / °	–	–	–	–	–	89.098(7)
V / Å^3	1681.47(9)	1693.89(13)	1685.52(5)	1669.58(11)	1664.4(4)	1604.2(2)
Z	2	2	2	2	2	2
μ / mm^{-1}	3.080	2.986	3.000	3.029	3.038	3.152
D_c / gcm^{-3}	1.538	1.456	1.464	1.478	1.482	1.538
measured reflections	7596	6514	13490	17110	16789	51778
independent reflections	1658	1689	1684	1683	1667	19048
R_{int}	0.033	0.026	0.033	0.044	0.062	–[a]
parameters	136	127	127	127	127	431
restraints	40	39	40	40	40	0
R_1 [$F_0 > 4\sigma(F_0)$][b]	0.073	0.065	0.050	0.053	0.094	0.064
wR_2, all data[c]	0.217	0.215	0.160	0.170	0.310	0.194
goodness of fit	1.056	1.125	1.113	1.147	1.336	1.022
$\Delta\rho_{min/max}$ / eÅ^{-3}	−0.62/0.77	−0.62/0.39	−0.46/0.29	−0.54/0.52	−0.95/1.76	−0.80/0.85
CCDC	2195223	2195224	2195225	2195226	2195227	2195228

[a]This dataset was resolved into four twin domains. [b]$R = \Sigma[|F_o| - |F_c|] / \Sigma|F_o|$ [c]$wR = [\Sigma w(F_o^2 - F_c^2) / \Sigma wF_o^4]^{1/2}$

Definitions of the structural parameters discussed in the paper

θ is the dihedral angle between the least squares planes of the two *L* ligands in a mononuclear $[ML_2]^{2+}$ complex, while ϕ is the *trans*-N{pyridyl}–Fe–N{pyridyl} bond angle (Scheme S1).[6,7] Significant changes to θ or (especially) ϕ during SCO are often associated with highly cooperative spin transitions, with significant thermal hysteresis.[7-9]

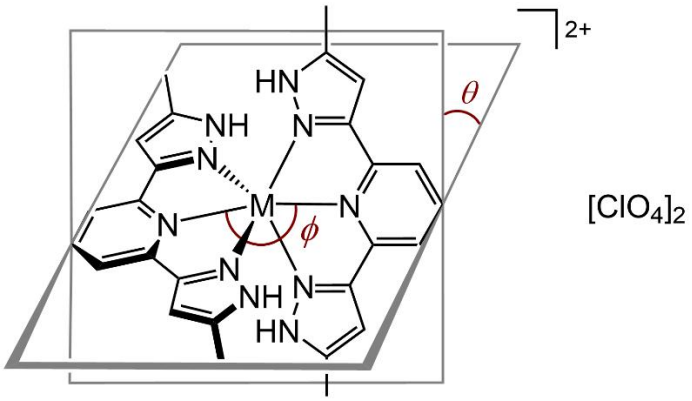

Scheme S1. The parameters θ and ϕ, which are used to discuss the structures of $[ML_2]^{2+}$ (M = Fe, Zn).

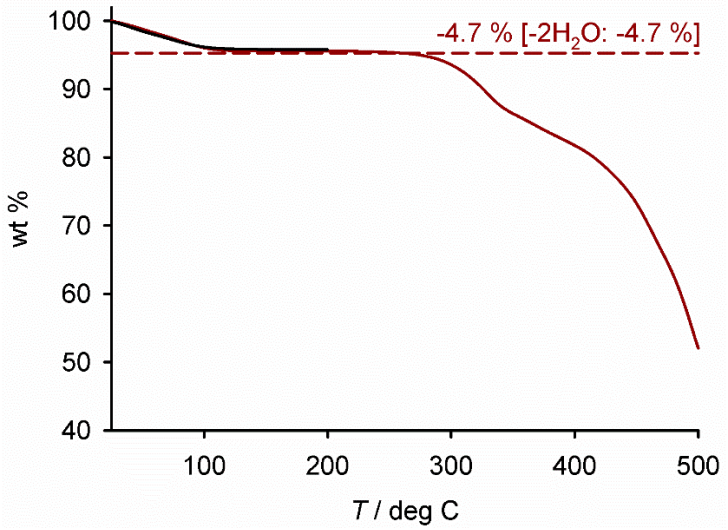

Figure S2 Thermogravimetric analysis (TGA) for **2b**·2H_2O (black). The material was only heated up to 200 °C, for safety reasons. Data for **2a**·2H_2O are also included (red), for comparison.[3]

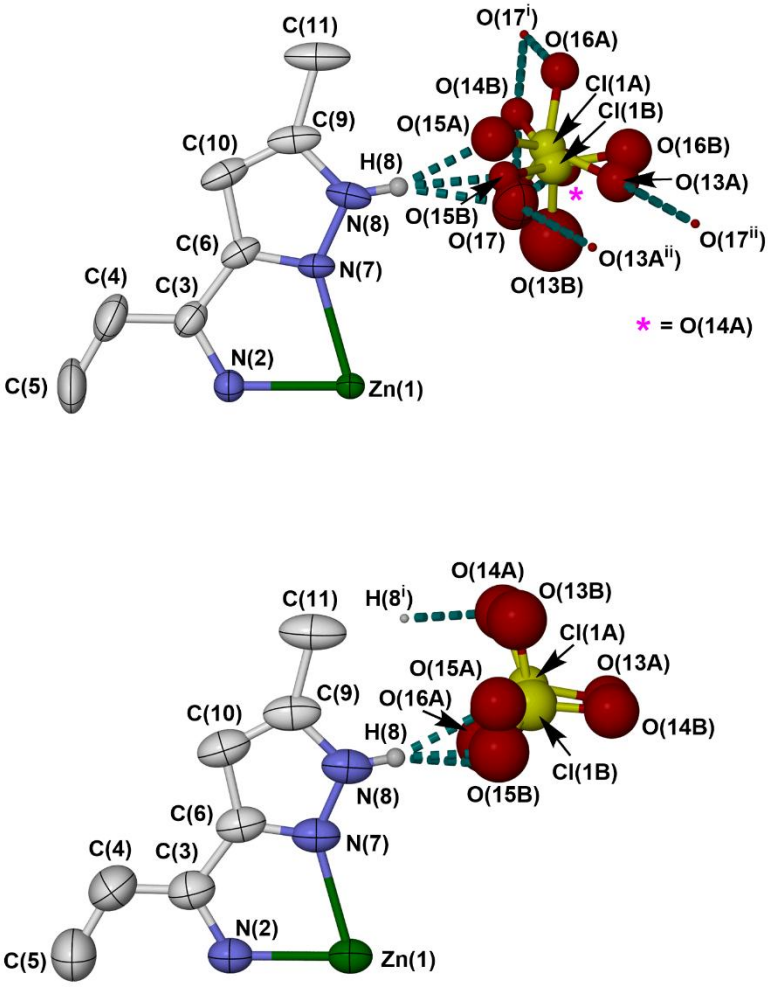

Figure S3 The asymmetric units of **2b**·2H_2O at 120 K (top) and **2b** phase B at 250 K (bottom), showing the full atom numbering schemes. Displacement ellipsoids are at the 50 % probability level, and C-bound H atoms are omitted for clarity. Symmetry codes: (i) $^3/_2-x$, $^1/_2-y$, z; (ii) $2-x$, $1-y$, $1-z$.

Colour code: C, white; H, pale grey; Cl, yellow; Zn, green; N, blue; O, red.

Atom O(16B) in **2b** phase B is obscured behind the Cl atom sites.

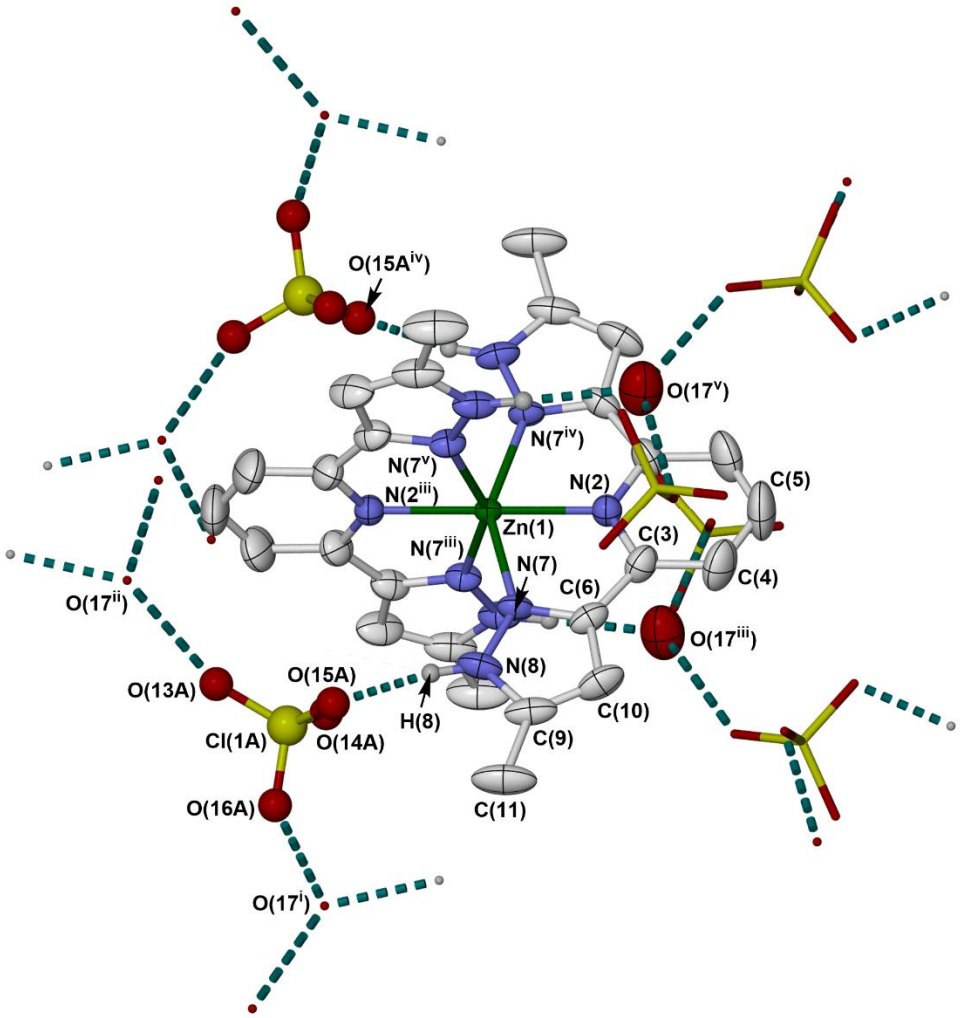

Figure S4 The complete formula unit of **2b**·2H_2O at 120 K, showing the hydrogen bonds in the lattice. Only the major orientation of the disordered half-anion is shown, and moieties that are not directly hydrogen bonded to the cation are de-emphasised for clarity. Displacement ellipsoids are at the 50 % probability level, where shown, and C-bound H atoms are omitted for clarity. Hydrogen atoms for the half-water molecule O(17) were not included in the refinement.

Colour code: C, white; H, pale grey; Cl, yellow; N, blue; O, red; Zn, green.

Symmetry codes: (i) $^{3}/_{2}-x$, $^{1}/_{2}-y$, z; (ii) $2-x$, $1-y$, $1-z$; (iii) y, $^{3}/_{2}-x$, $^{1}/_{2}-z$; (iv) $^{3}/_{2}-x$, $^{3}/_{2}-y$, z; (v) $^{3}/_{2}-y$, x, $^{1}/_{2}-z$.

The half-anion and half-water molecule are disordered about the same lattice cavity, so the hydrogen bond network is in fact disordered within the crystal.

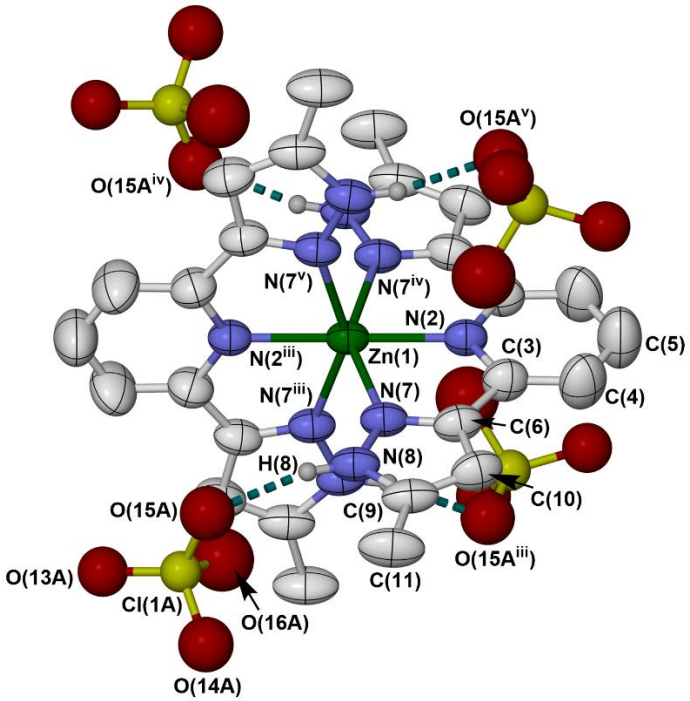

Figure S5 The complete formula unit of phase B of **2b** at 250 K, showing the hydrogen bonds in the lattice. Only one orientation of the disordered half-anion is shown. Displacement ellipsoids are at the 50 % probability level, and C-bound H atoms are omitted for clarity.

Colour code: C, white; H, pale grey; Cl, yellow; N, blue; O, red; Zn, green.

Symmetry codes: (iii) y, $^{3}/_{2}-x$, $^{1}/_{2}-z$; (iv) $^{3}/_{2}-x$, $^{3}/_{2}-y$, z; (v) $^{3}/_{2}-y$, x, $^{1}/_{2}-z$.

The disordered (half)-anions are themselves disordered across a crystallographic C_2 axis, which randomly distributes them between hydrogen-bond donor groups on two different cations (Figure S7).

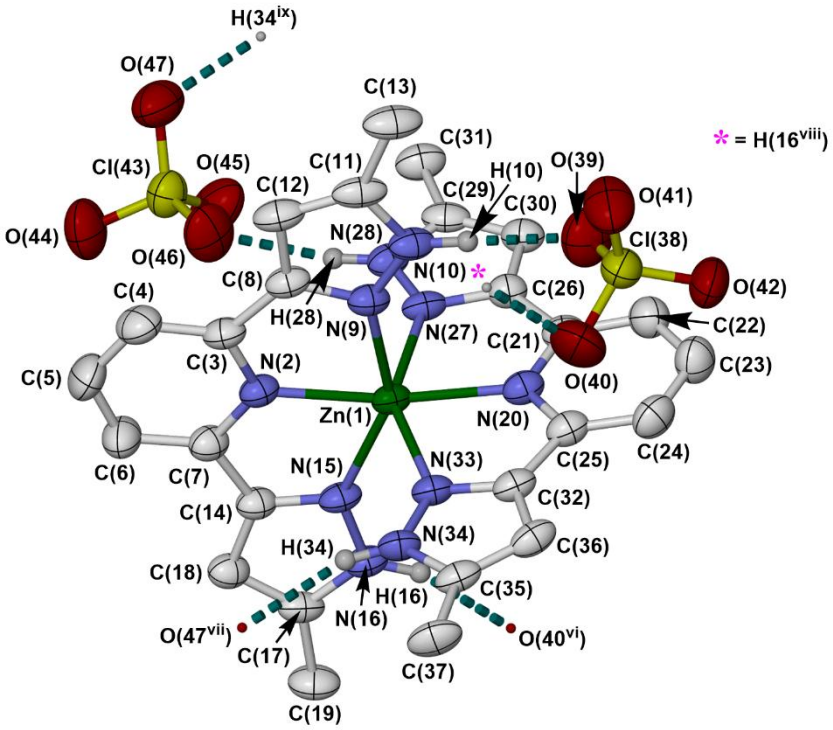

Figure S6 The asymmetric unit of phase C of **2b** at 120 K. Displacement ellipsoids are at the 50 % probability level, and C-bound H atoms are omitted for clarity.

Colour code: C, white; H, pale grey; Cl, yellow; N, blue; O, red; Zn, green.

Symmetry codes: (vi) *x*, 1+*y*, *z*; (vii) −1+*x*, *y*, *z*; (viii) *x*, −1+*y*, *z*; (ix) 1+*x*, *y*, *z*.

Table S2 Selected bond lengths and angles in the crystal structure of **2b**·2H$_2$O and **2b** (Å, º). See Figs. S4-S6 for the atom numbering scheme employed, and Scheme S1 for the definitions of ϕ and θ. Symmetry codes: (iii) y, $^3/_2-x$, $^1/_2-z$; (iv) $^3/_2-x$, $^3/_2-y$, z; (v) $^3/_2-y$, x, $^1/_2-z$.

	2b·2H$_2$O	**2b**, phase B				**2b**, phase C	
T (K)	120	350	300	250	200		120
Zn(1)–N(2)	2.110(5)	2.092(5)	2.098(4)	2.099(4)	2.096(7)	Zn(1)–N(2)	2.104(2)
Zn(1)–N(7)	2.179(3)	2.222(3)	2.220(2)	2.216(2)	2.226(3)	Zn(1)–N(9)	2.235(2)
						Zn(1)–N(15)	2.181(2)
						Zn(1)–N(20)	2.095(2)
						Zn(1)–N(27)	2.214(3)
						Zn(1)–N(33)	2.187(2)
N(2)–Zn(1)–N(7)	74.51(10)	74.48(9)	74.46(7)	74.50(7)	74.33(11)	N(2)–Zn(1)–N(9)	73.91(9)
						N(2)–Zn(1)–N(15)	74.90(9)
N(2)–Zn(1)–N(2^{iii})	180	180	180	180	180	N(2)–Zn(1)–N(20)	168.09(9)
N(2)–Zn(1)–N(7^{iii})	105.49(10)	105.52(9)	105.54(7)	105.50(7)	105.67(11)	N(2)–Zn(1)–N(27)	105.57(9)
						N(2)–Zn(1)–N(33)	105.24(10)
N(7)–Zn(1)–N(7^{iv})	149.0(2)	148.96(18)	148.91(14)	149.00(15)	148.7(2)	N(9)–Zn(1)–N(15)	148.59(9)
						N(9)–Zn(1)–N(20)	94.18(9)
N(7)–Zn(1)–N(7^{v})	94.09(5)	94.11(5)	94.12(4)	94.09(4)	94.19(6)	N(9)–Zn(1)–N(27)	93.83(9)
						N(9)–Zn(1)–N(33)	91.53(9)
						N(15)–Zn(1)–N(20)	116.99(9)
						N(15)–Zn(1)–N(27)	97.99(9)
						N(15)–Zn(1)–N(33)	93.06(9)
						N(20)–Zn(1)–N(27)	74.56(10)
						N(20)–Zn(1)–N(33)	74.62(10)
						N(27)–Zn(1)–N(33)	149.01(9)
ϕ	180	180	180	180	180	ϕ	168.09(9)
θ	90	90	90	90	90	θ	89.23(2)

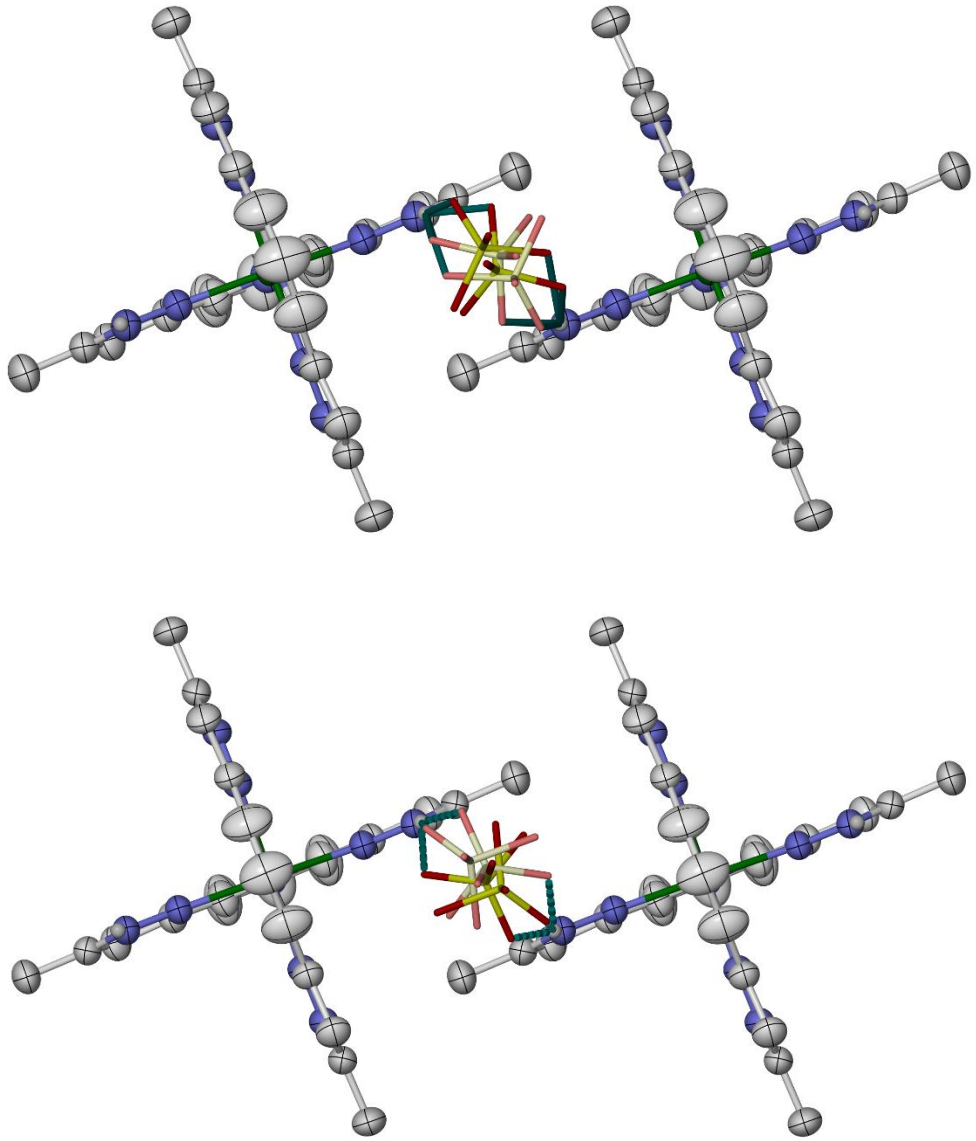

Figure S7 The full anion disorder in phase B of **2b** at 300 K (top) and 250 K (bottom). Displacement ellipsoids are at the 50 % probability level except for the anion, which is de-emphasised for clarity. C-bound H atoms are not included.

Colour code: C, white; H, pale grey; Cl, yellow; N, blue; O, red; Zn, green. The two disorder orientations associated with the symmetry-related half-anion sites, related by the operation $^{3}/_{2}-x$, $^{1}/_{2}-y$, z, are shown with dark and pale colouration.

The anion disorder is the same at 350 and 300 K; and, at 250 and 200 K. However the refinements imply the disordered anions reorient themselves between 300 and 250 K, which changes the pattern of hydrogen bonding.

- At 350 and 300 K, all four partial anions form hydrogen bonds to both cations.
- At 250 and 200 K, one partial anion (and its symmetry equivalent) hydrogen bond to both cations, but the other partial anion hydrogen bonds to just one cation site.

While the level of disorder means it must be interpreted with caution, such a rearrangement of the anions could be a precursor to the phase B→C transformation which occurs below 200 K.

Table S3 Hydrogen bond parameters in the structures of **2b**·2H$_2$O and **2b** (Å, °). See Figs. S4-S6 for the atom numbering scheme employed. Symmetry codes in this Table are listed in Table S3. Symmetry codes: (i) $^3/_2-x$, $^1/_2-y$, z; (ii) $2-x$, $1-y$, $1-z$; (vi) x, $1+y$, z; (vii) $-1+x$, y, z.

	D−H	H…A	D…A	D−H…A
2b·2H$_2$O (120 K)				
N(8)–H(8)···O(15A)/O(15B)	0.88	1.92/1.95	2.756(13)/2.80(3)	159.3/163.8
N(8)–H(8)···O(17)	0.88	2.12	2.955(13)	158.7
O(17)···O(16A^{i})/O(14B^{i})	–[a]	–[a]	2.738(15)/2.61(2)	–[a]
O(17)···O(13A^{ii})	–[a]	–[a]	2.932(15)	–[a]
2b, phase B (350 K)				
N(8)–H(8)···O(15A)/O(15B)	0.86	2.35/2.27	3.05(2)/3.07(2)	138.4/155.5
N(8)–H(8)···O(16A^{i})/O(16B^{i})	0.86	1.82/2.16	2.681(19)/2.960(19)	176.6/154.4
2b, phase B (300 K)				
N(8)–H(8)···O(15A)/O(15B)	0.86	2.30/2.12	3.011(17)/2.940(19)	140.1/158.2
N(8)–H(8)···O(16A^{i})/O(16B^{i})	0.86	1.85/2.17	2.704(14)/2.955(14)	172.7/152.0
2b, phase B (250 K)[b]				
N(8)–H(8)···O(15A)/O(15B)	0.86	2.04/1.76	2.875(15)/2.618(15)	162.6/172.0
N(8)–H(8)···O(14A^{i})	0.86	2.13	2.881(14)	144.9
2b, phase B (200 K)[b]				
N(8)–H(8)···O(15A)/O(15B)	0.88	2.00/1.79	2.86(2)/2.653(19)	162.8/167.8
N(8)–H(8)···O(14A^{i})	0.88	2.18	2.93(2)	143.1
2b, phase C (120 K)				
N(10)–H(10)···O(39)	0.88	1.98	2.838(4)	165.7
N(16)–H(16)···O(40^{vi})	0.88	2.30	3.053(5)	144.2
N(28)–H(28)···O(46)	0.88	2.15	2.931(4)	148.4
N(34)–H(34)···O(47^{vii})	0.88	2.09	2.896(4)	151.6

[a]The H atoms on the water half-molecule O(17) were not included in the crystallographic refinement.
[b]There is a rearrangement of the disordered anion sites between 300 and 250 K, which changes the geometry of the N−H···O hydrogen bonds (Figure S7).

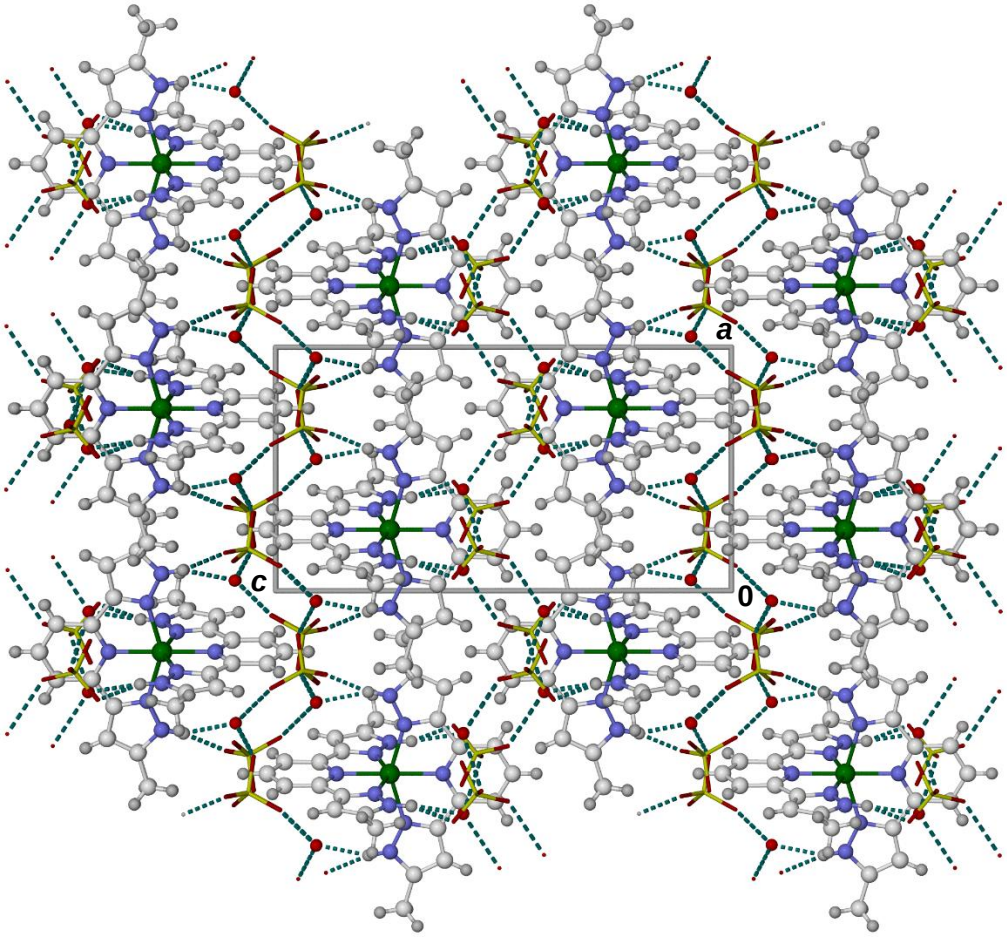

Figure S8 Packing diagram of **2b**·2H_2O, viewed along the (010) crystal vector. Only the 'A' disorder orientation of the half-anion is included, but both symmetry equivalents for each anion and water site are shown. The ClO_4^- ions are de-emphasised for clarity.

Colour code: C, white; H, pale grey; Cl, yellow; N, blue; O, red; Zn, green.

The half-water molecule H atoms were not included in the refinement, and so are not shown in the Figure. Hydrogen bonds donated by the water molecule O(17) are shown as O···O contacts.

Each anion and water site in the Figure is half-occupied, from symmetry-imposed disorder about a crystallographic C_2 axis. So, only half the ClO_4^- ions, water molecules and hydrogen bonds in the Figure are actually present in practise, and are randomly distributed through the lattice.

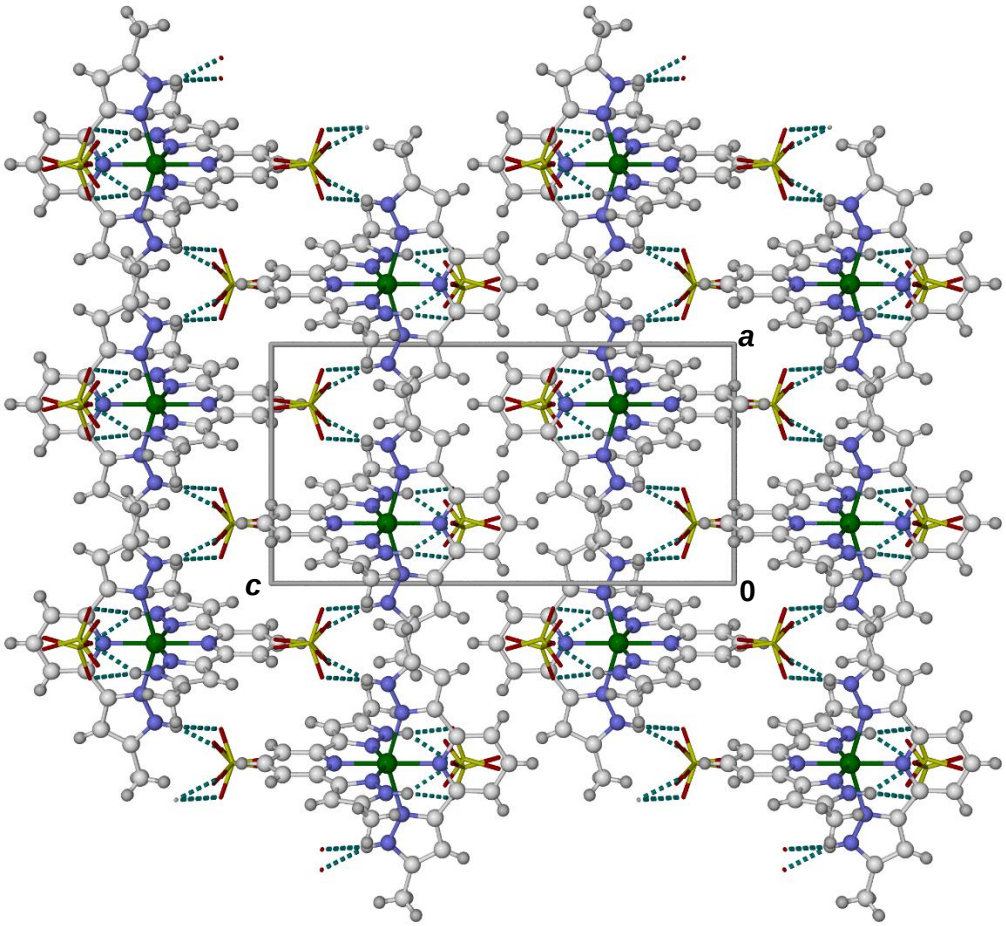

Figure S9 Packing diagram of **2b** phase B at 250 K, viewed along the (010) crystal vector. Only the 'A' disorder orientation of the half-anion is included, but both symmetry equivalents for each anion site are shown which are de-emphasised for clarity.

Colour code: C, white; H, pale grey; Cl, yellow; N, blue; O, red; Zn, green.

Each anion in the Figure is half-occupied, from symmetry-imposed disorder about a crystallographic C_2 axis. So, only half the anions and hydrogen bonds in the Figure are actually present in practise, in a random distribution through the lattice.

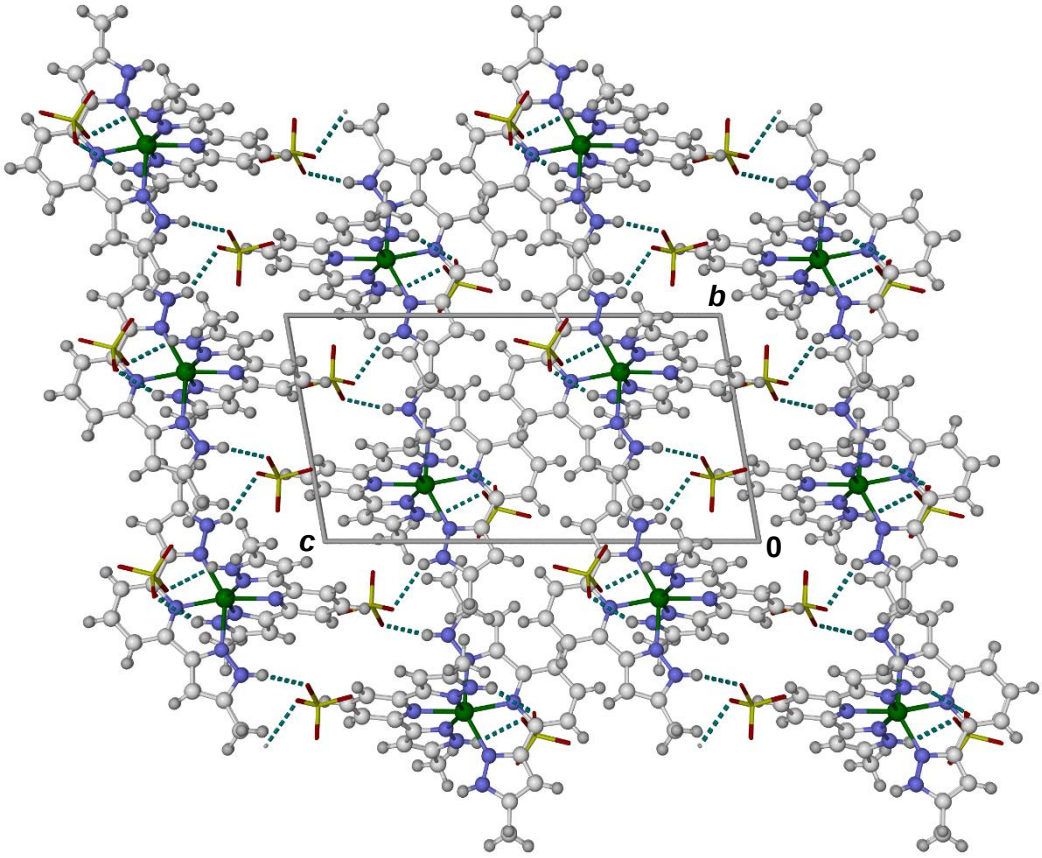

Figure S10 Packing diagram of phase C of **2b** at 120 K, viewed along the (100) crystal vector. The ClO_4^- ions are de-emphasised for clarity.

Colour code: C, white; H, pale grey; Cl, yellow; N, blue; O, red; Zn, green.

There is no symmetry-imposed crystallographic disorder in this phase.

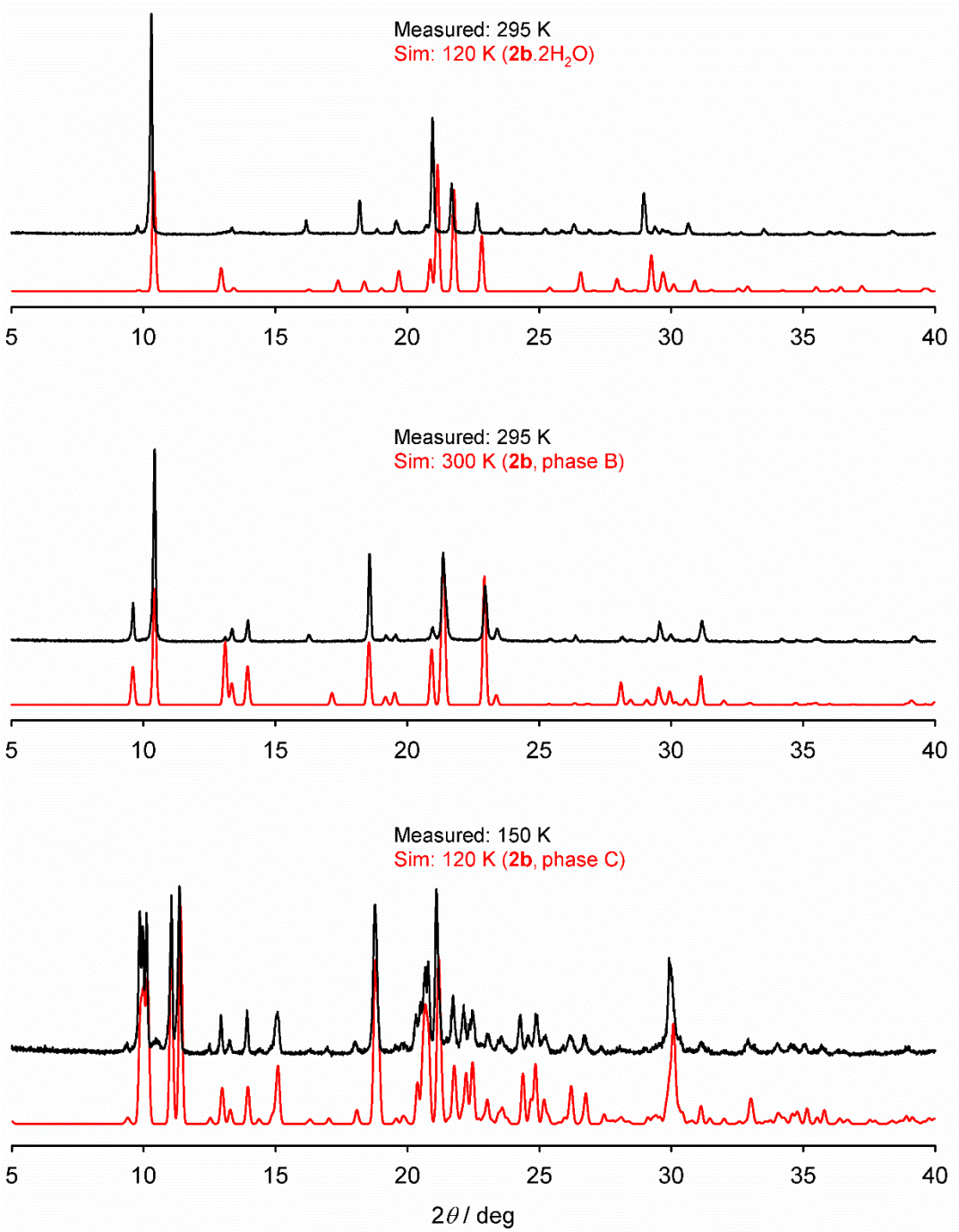

Figure S11 Comparison of measured (black) and simulated (red) powder diffraction data for **2b**·2H_2O and the two phases of **2b**.

The small 2θ offset between the measured and simulated peaks for **2b**·2H_2O can be attributed to the very different temperatures of the two measurements. Otherwise, the agreement between experiment and simulation is very good, with the two small caveats below.

The peak at 2θ = 16.3° shown by **2b**·2H_2O, which has a weak counterpart in the simulation for that phase, is retained in the phase B powder pattern but not in its simulation. The reason for that small discrepancy is unclear.

The weak residual peak at 2θ = 10.5° in the phase C powder pattern suggest a small fraction of the sample retains phase B below the nominal phase transition temperature. That was also observed in powder diffraction measurements of **1b** (Figure 4, main article),[2] as well as **1a** and **2a**.[3]

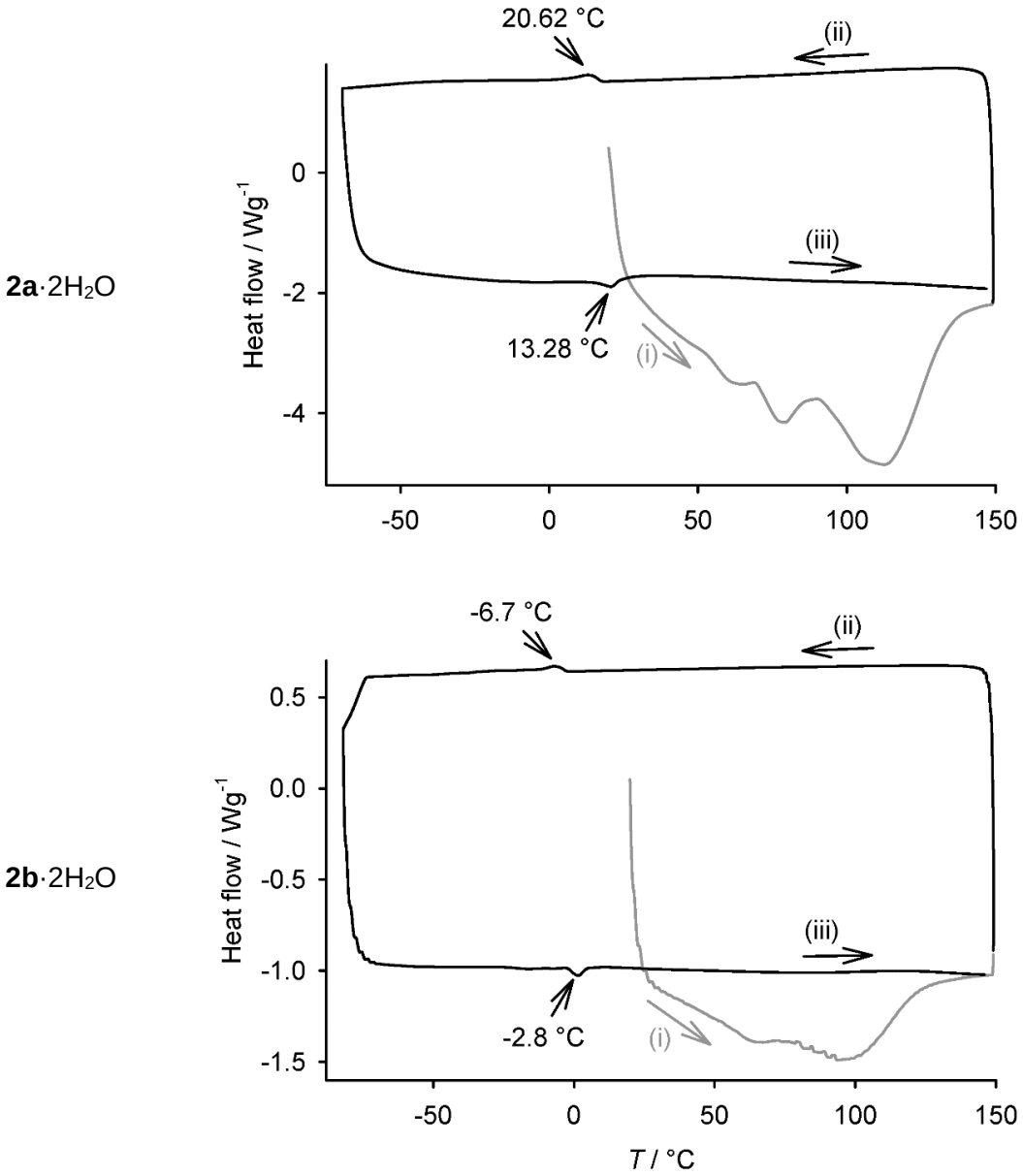

2a·2H₂O

2b·2H₂O

Figure S12 Differential scanning calorimetry (DSC) data for **2a**·2H₂O (top) and **2b**·2H₂O (bottom), at a scan rate of 10 Kmin^{-1}. The temperature ramps are: (i) 20 → 149 °C; (ii) 149 → –70 °C; (iii) –70 → 147 °C. Data for **2a**·2H₂O are taken from ref. 3.

The initial warming ramps (grey trace) show strong endotherms arising from the dehydration of the samples (Figure S2). Scans (ii) and (iii) (black) arise from the dehydrated materials.

The highlighted features in scans (ii) and (iii) of **2a** are unambiguously assigned to the phase B→C transformation, as their temperature (average 290 K) coincides well with the phase transition measured crystallographically and by powder diffraction.[3]

The average temperature of the corresponding peaks for **2b** (268 K) is consistent with the onset of the phase B→C transition on cooling in the powder diffraction measurement (Figure 3, main article). However, there is no evidence in the DSC data for the broadening of the phase transition observed by powder diffraction, which occurs over a 25±5 K temperature window in that experiment. There is no evidence for broadening of the phase transition in the DSC trace.

The different characteristics for the phase B→C transition in **2b** measured by crystallography, powder diffraction and DSC imply it depends on the measurement conditions and/or the history of the sample.

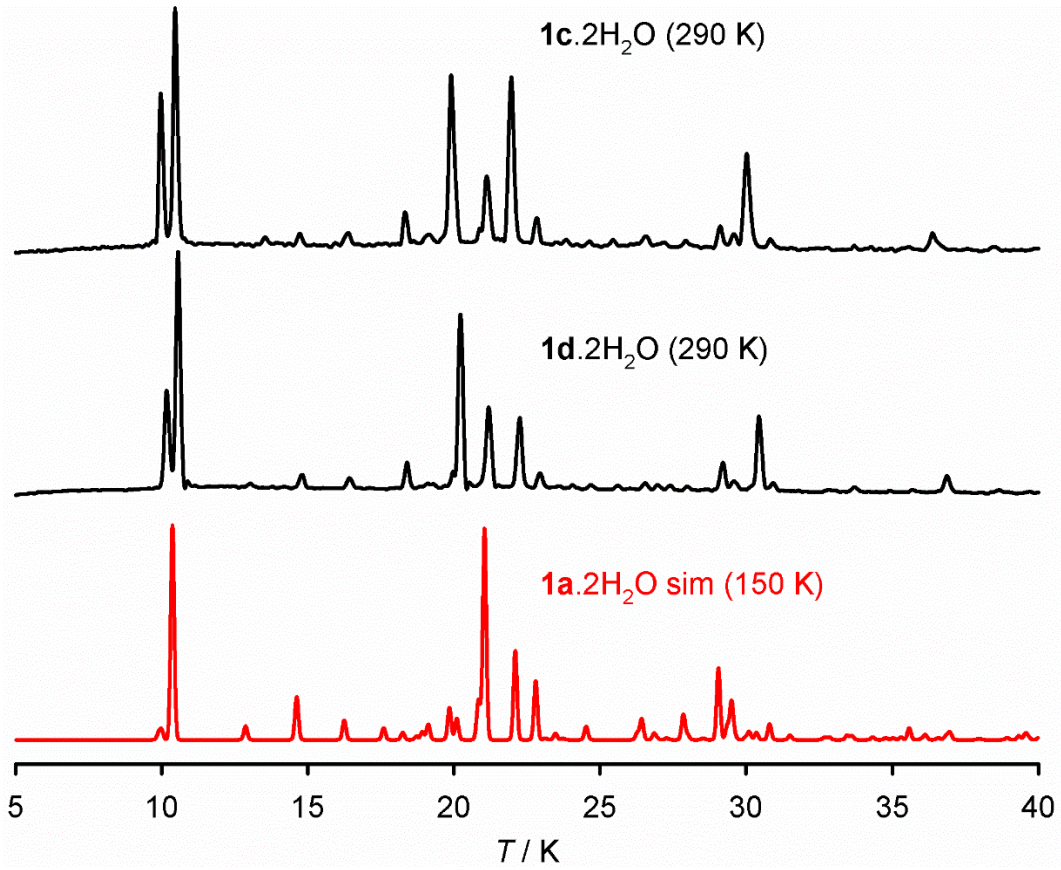

Figure S13 Measured room temperature powder diffraction data for **1c**·2H_2O and **1d**·2H_2O (black), and a simulation based on the structure of **1a**·2H_2O at 150 K (red).[1]

Differences in peak intensities between the measurement and simulation arise from preferred orientation in the ground polycrystalline samples. However, there is good correspondence of the peak positions in the measurements and simulation, allowing for the different compositions of the samples and the low temperature of the simulation.

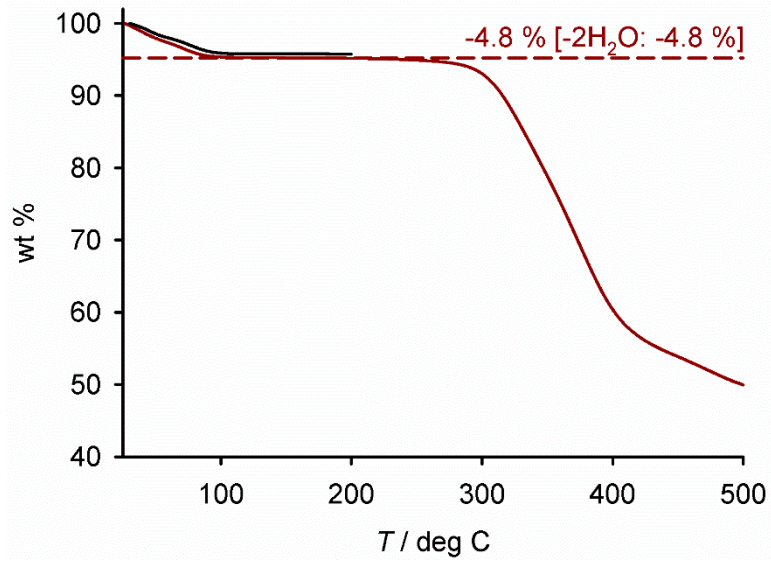

Figure S14 Thermogravimetric analysis (TGA) for **1c**·2H_2O (black) and **1d**·2H_2O (gray). The materials were only heated up to 200 °C, for safety reasons. Data for **1a**·2H_2O are included (red), for comparison.[3]

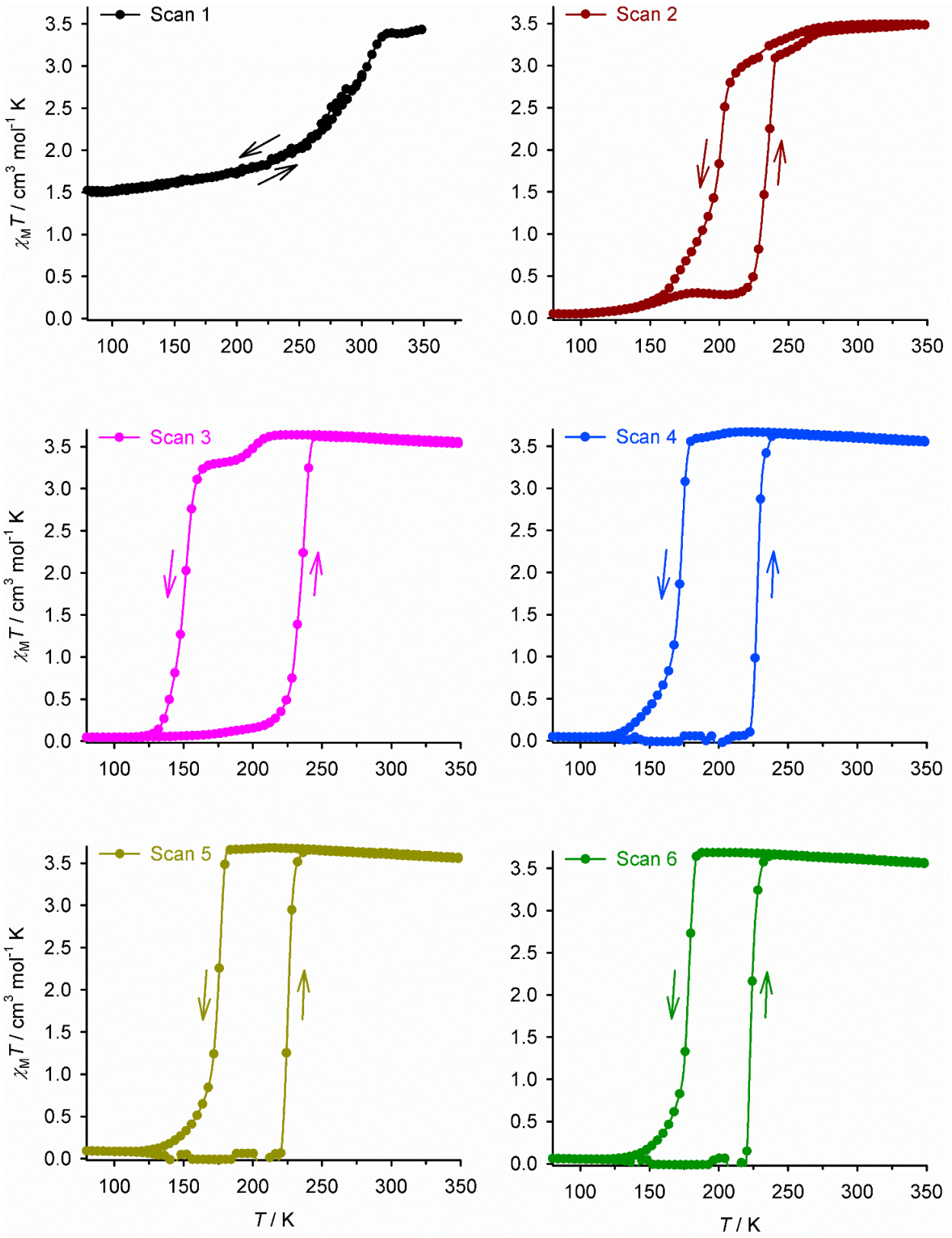

Figure S15 The individual magnetic susceptibility scans from Figure 5 (main article) for **1c**·2H_2O (scan 1) and **1c** (scans 2-6). Data points are linked by spline curves for clarity. Scan rate 2 K min^{-1}.

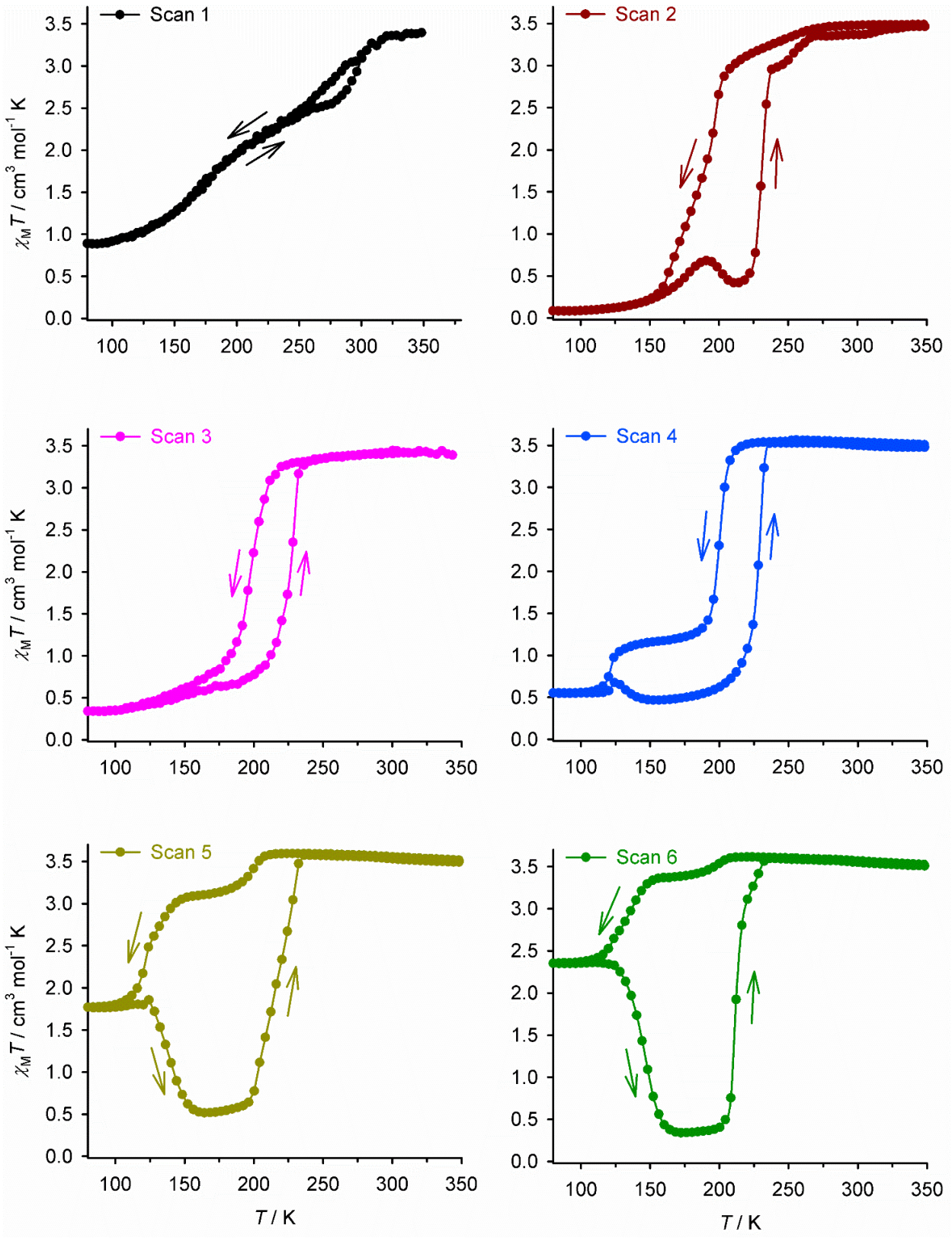

Figure S16 The individual magnetic susceptibility scans from Figure 5 (main article) for **1d**·2H_2O (scan 1) and **1d** (scans 2-6). Data points are linked by spline curves for clarity. Scan rate 2 K min^{-1}.

Notwithstanding the TIESST in **1d**, in other respects scan 3 of **1c** (Figure S15) and scans 5 and 6 of **1d**, closely resemble each other. Additional scanning of **1c** causes its evolution to a symmetrical spin-transition hysteresis loop, whereas **1d** remains trapped in that intermediate state under the same conditions. This is discussed in the main article.

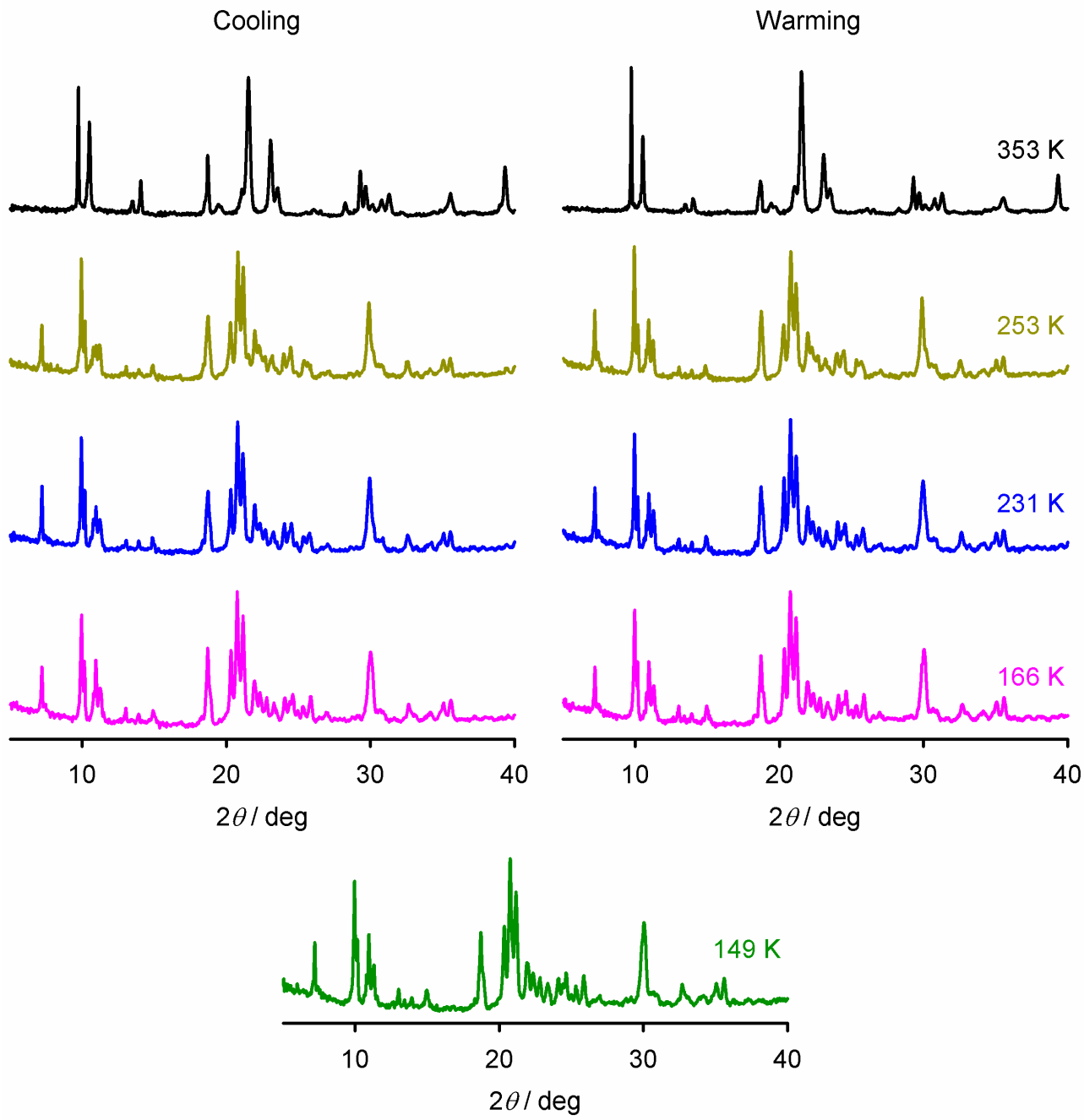

Figure S17 Powder diffraction patterns on cooling and warming temperature ramps, for anhydrous **1d**, produced by *in situ* dehydration of **1d**·2H_2O (Figure S13).

The sample adopts phase B at 353 K, and phase C at the other temperatures (compare with Figure S11). There is no obvious temperature dependence of the phase C powder pattern, which resembles the behaviour shown by **1b** and **2b** (Figure 3, main article). That contrasts with **1a** and **2a**, whose phase C powder patterns are strongly temperature-dependent.[3]

The sample has not transformed to its thermodynamic low-spin phase (phase E) at 149 K, the lowest temperature achieved on this diffractometer.[1,3] It is unclear how that correlates with the spin state properties of forms (i) and (ii) of **1d** (Figure S16 and Scheme 2, main article).

Multiple thermal scans of this material on the powder diffractometer were not achieved, because of instrument time constraints. However, on this evidence the complicated sequence of transformations in the magnetic data for **1d** is not reflected in its powder pattern, which shows the same phase behaviour as the anion-pure salts **1a** and **1b**.

References

1 T. D. Roberts, F. Tuna, T. L. Malkin, C. A. Kilner and M. A. Halcrow, *Chem. Sci.*, 2012, **3**, 349–354.

2 T. D. Roberts, M. A. Little, F. Tuna, C. A. Kilner and M. A. Halcrow, *Chem. Commun.*, 2013, **49**, 6280–6282.

3. C. M. Pask, S. Greatorex, R. Kulmaczewski, A. Baldansuren, E. J. L. McInnes, F. Bamiduro, M. Yamada, N. Yoshinari, T. Konno and M. A. Halcrow, *Chem. – Eur. J.*, 2020, **26**, 4833–4841.

4. G. M. Sheldrick, *Acta Cryst. Sect. C.: Struct. Chem.*, 2015, **71**, 3–8.

5 L. J. Barbour, *J. Appl. Crystallogr.*, 2020, **53**, 1141–1146.

6 O. V. Dolomanov, L. J. Bourhis, R. J. Gildea, J. A. K. Howard and H. Puschmann, *J. Appl. Crystallogr.*, 2009, **42**, 339–341.

7 J. M. Holland, J. A. McAllister, C. A. Kilner, M. Thornton-Pett, A. J. Bridgeman and M. A. Halcrow, *J. Chem. Soc. Dalton Trans.*, 2002, 548–554.

8 M. A. Halcrow, *Coord. Chem. Rev.*, 2009, **253**, 2493–2514.

9 L. J. Kershaw Cook, F. L. Thorp-Greenwood, T .P. Comyn, O. Cespedes, G. Chastanet and M. A. Halcrow, *Inorg. Chem.*, 2015, **54**, 6319−6330.

10 a) K. S. Kumar, B. Heinrich, S. Vela, E. Moreno-Pineda, C. Bailly and M. Ruben, *Dalton Trans.*, 2019, **48**, 3825–3830;
b) N. Suryadevara, A. Mizuno L. Spieker S. Salamon, S. Sleziona, A. Maas, E. Pollmann, B. Heinrich, M. Schleberger, H. Wende, S. K. Kuppusamy and M. Ruben, *Chem. – Eur. J.*, 2022, **28**, e202103853.

11 A. J. Gordon and R. A. Ford, *The Chemists Companion – A Handbook of Practical Data, Techniques and References*, John Wiley, Chichester, 1972, p. 109.